NANO LETTERS

pubs.acs.org/NanoLett Letter

Metamaterial-Assisted Photobleaching Microscopy with Nanometer Scale Axial Resolution

Yeon Ui Lee, Junxiang Zhao, Gary C. H. Mo, Shilong Li, Guangru Li, Qian Ma, Qingqing Yang, Ratnesh Lal, Jin Zhang, and Zhaowei Liu*

Cite This: https://dx.doi.org/10.1021/acs.nanolett.0c02056 Read Online

ACCESS | Metrics & More | Article Recommendations | Supporting Information

ABSTRACT: The past two decades have witnessed a dramatic progress in the development of novel super-resolution fluorescence microscopy technologies. Here, we report a new fluorescence imaging method, called metamaterial-assisted photobleaching microscopy (MAPM), which possesses a nanometer-scale axial resolution and is suitable for broadband operation across the entire visible spectrum. The photobleaching kinetics of fluorophores can be greatly modified via a separation-dependent energy transfer process to a nearby metamaterial. The corresponding photobleaching rate is thus linked to the distance between the fluorophores and the metamaterial layer, leading to a reconstructed image with exceptionally high axial resolution. We apply the MAPM technology to image the HeLa cell membranes tagged with fluorescent proteins and demonstrate an axial resolution of ~2.4 nm with multiple colors. MAPM utilizes a metamaterial-coated substrate to achieve super-resolution without altering anything else in a conventional microscope, representing a simple solution for fluorescence imaging at nanometer axial resolution.

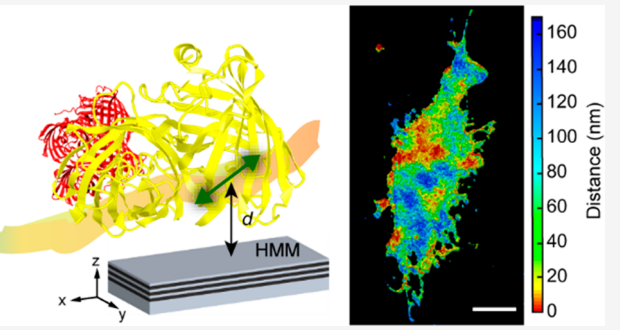

KEYWORDS: *Super-resolution imaging, Metamaterial, Photobleaching microscopy, Purcell effect, Nanophotonics, Plasmonics*

Optical microscope was invented in the 17th century to examine minute features of specimens through the magnification of a set of lenses with visible light and is still widely used today. Although optical microscopes are indispensable in many fields, their lateral and axial resolutions are limited by the diffraction limits which are about 250 nm and about 800 nm, respectively.[1,2] In the past two decades, various super-resolution fluorescence microscopic techniques such as stimulated emission depletion (STED),[3] ground state depletion (GSD),[4] the photoactivated localization microscopy (PALM),[5] and stochastic optical reconstruction microscopy (STORM),[6] have achieved a lateral resolution on the order of tens of nanometers in routine measurements, and were applied for various biological studies. Structured illumination microscopy (SIM),[7,8] on the other hand, only improves the resolution by roughly a factor of two compared to diffraction limit. However, its high-speed capability leads to tremendous enthusiasms in life cell imaging.

These super-resolution fluorescence microscopy techniques have been combined with various other techniques to achieve multicolor three-dimensional (3D) super-resolution imaging of cellular structures. For example, 4Pi-RESOLFT[9] utilizes dual-objective 4Pi detection to achieve ~50/50 nm lateral/axial resolution; STORM combined with single cylindrical lens,[1] double cylindrical lenses,[10] and self-bending point spread function methods[11] can achieve lateral/axial resolution of ~20/50 nm, ~10/20 nm, and ~13/15 nm, respectively; iPALM[12,13] utilizes simultaneous multiphase interferometry and provides lateral/axial resolution of ~10/10 nm. Despite all the impressive progress, current multicolor 3D super-resolution techniques still face technical challenges to reach both the lateral and axial resolutions below 10 nm. Moreover, the required complex optical setup of these techniques limits wide applications in practice.

Recent years have seen a boom of near-field optics and metal plasmonics has become an inevitable requirement of subwavelength light control. It has widely been demonstrated that the electromagnetic near-field of fluorescent emitters close to the metal couples to surface plasmon polaritons (SPPs) of the metal film, transferring energy from excited molecules to the metal, similar to Fürster resonant energy transfer (FRET).[14] The lifetime of the fluorophore is thus modified by the energy transfer process, which is very sensitive to the distance between the fluorophore and the metal film. As a consequence, the axial information on the fluorophore can be

Received: May 14, 2020
Revised: June 22, 2020
Published: June 29, 2020

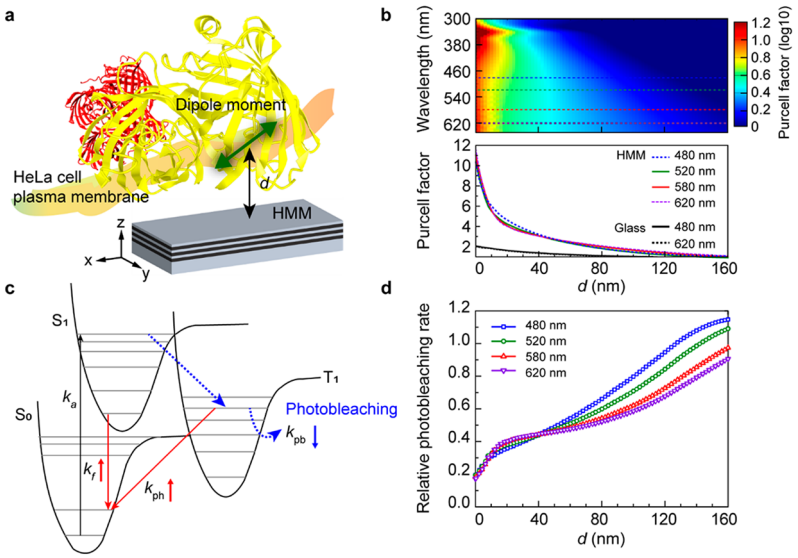

Figure 1. Metamaterial-assisted photobleaching response. (a) Schematic illustration (not to scale) of a fluorescence protein in a HeLa cell membrane on top of an HMM substrate. The fluorescence protein can be treated as a dipole emitter, which is away from the HMM surface with an axial distance *d*. The HMM multilayer consists of three pairs of Ag/SiO_2 bilayer with thickness of 10/4 nm. (b) Calculated Purcell factor as a function of the emission wavelength of the dipole emitter and its axial distance from the HMM (a), showing a wide broadband response and a strong axial-distance dependence. The bottom panel shows the axial-distance dependence of the Purcell factor for the dipole emitter on top of the HMM and a glass substrate at the wavelengths of 480, 520, 580, and 620 nm, respectively. (c) Simplified Jablonski energy diagram for the photobleaching kinetics. Details are shown in SI. (d) Calculated axial-distance dependence of the relative photobleaching rate of the fluorescence protein over the HMM substrate.

gained by introducing a metal film. For example, Chizhik and co-workers have recently developed such a method to improve the axial resolution based on fluorescence lifetime imaging microscope (FLIM), which is termed as metal-induced energy transfer (MIET).[15−18] However, apart from the strict requirement for lifetime measurements on the nanosecond time scale, broadband multicolor imaging might be challenging for MIET because the SPP resonance is typically a narrow band phenomenon.

Metamaterials[19,20] are artificially engineered media made by composite structures consisting of deep subwavelength-sized components and offer extraordinary material properties that not readily obtained from conventional media. Hyperbolic metamaterial (HMM)[21,22] is one of the most practical metamaterials at visible frequencies and is typically fabricated by stacking metal/dielectric multilayers. HMMs have been used to achieve super resolution imaging in hyperlens[23,24] and also for broadband spontaneous emission enhancement due to the Purcell effect.[22,25−28] As a result, in contrast to the single layer of metal film[16,29] used in MIET, a slab of HMM can be designed to optimize the Purcell factor at desired working frequencies.[26,30] Therefore, the engineered HMMs represent a unique material platform for multicolor super-resolution imaging along the axial direction. It is worth noting that the precise determination of the axial location of fluorophores on the HMMs does not require the lifetime measurement on the nanosecond time scale, as we demonstrated below.

In this work, we propose and experimentally demonstrate a new fluorescence imaging method termed as metamaterial-assisted photobleaching microscopy (MAPM) that offers an axial resolution down to ∼2.4 nm over a wide range of colors. In MAPM, the multicolor subten-nanometer axial resolution is enabled by the Purcell-factor-modified photobleaching dynamics of fluorophores on top of HMMs. Figure 1a shows the schematic illustration of a fluorescence protein as a dipole emitter in a HeLa cell plasma membrane located on top of a HMM substrate with distance *d*. Photobleaching is a process in which the total number of ground state fluorophore is depleted via permanent photochemical destruction when the fluorophores are either in the singlet or the triplet excited state. Those bleached fluorophores can no longer participate in the excitation−emission cycle.[31] The core idea of our MAPM method is that the HMM provides strong enhancement of the local density of state (LDOS) of light in broadband spectrum resulting from the deep subwavelength confinement of light near the HMM.[26,32,33] The enhanced LDOS of light leads to enhanced spontaneous emission rate k_f of fluorophores near the HMM, that is, broadband Purcell enhancement which can be translated as photobleaching rate reduction as a function of the axial distance *d* of a fluorophore. (Figure 1b).

To find the axial-distance dependence of photobleaching lifetime used in MAPM, the widely used photobleaching model[34,35] is applied for the fluorophores-HMM system (see Supporting Information S1). The physics behind the model can be seen by the Jablonski energy diagram of a fluorophore shown in Figure 1c, which shows that both increments of the photoluminescence decay rate k_f and the phosphorescence decay rate k_{ph} result in the reduction of the probability of the fluorophore entering the bleaching channel. A giant suppression of photobleaching via the enhancement of LDOS on a plasmonic substrate has been reported.[36−40] The same is true for the HMM substrate used in MAPM, and the results are summarized in Figure 1d. The use of HMM instead of a single metallic substrate or other plasmonic substrates provides enhanced Purcell factor in broadband[22,26,32] (Figure S4) resulting in prominent broadband photobleaching reduction depending on the axial-distance. Therefore, this axial-distance-dependent photobleaching lifetime enables us to map the fluorophores' axial locations with exceptionally high

https://dx.doi.org/10.1021/acs.nanolett.0c02056
Nano Lett. XXXX, XXX, XXX−XXX

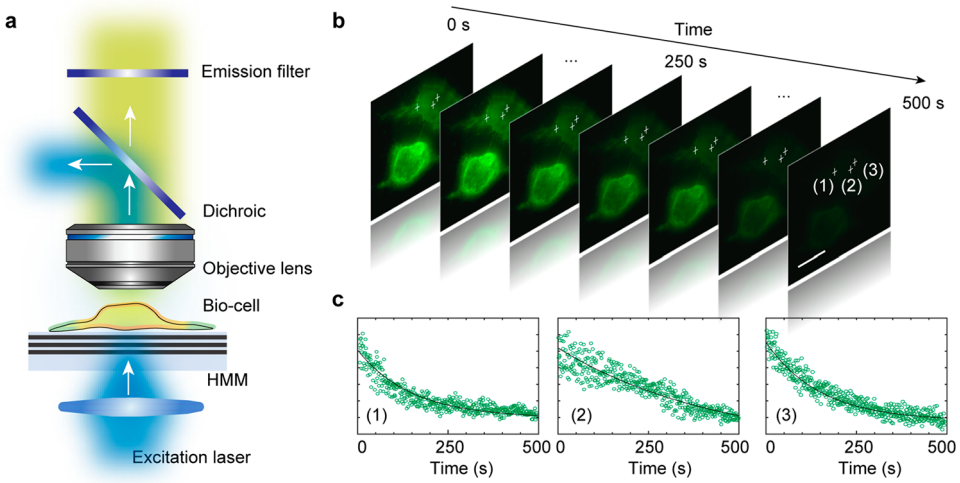

Figure 2. Metamaterial-assisted photobleaching microscopy. (a) Schematic showing the MAPM configuration. The MAPM experiments are based on a common fluorescence microscope, where the only modification is to insert a flat HMM layer between the cell and glass slide, making this imaging method extremely easy to implement. (b) Typical MAPM image sequences. The bleaching of the fluorescent signals is clearly visible over time. (c) Photobleaching decay curves for a few pixels in (b). The photobleaching lifetime for a given pixel is obtained by fitting the decay curve. The excitation laser wavelength is 488 nm, and the detection wavelength is 520 ± 20 nm.

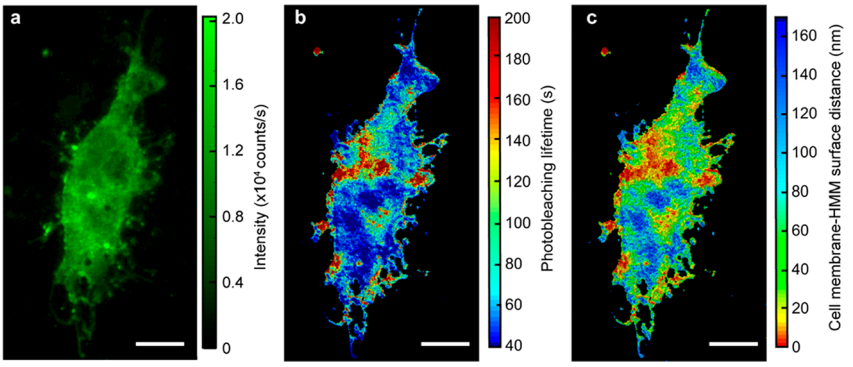

Figure 3. MAPM images of Hela cells. (a) Fluorescence intensity image of a Hela cell. (b) Photobleaching-lifetime image of the HeLa cell by MAPM reconstruction. (c) Super-axial-resolution image of the Hela cell showing the distance between the cell membrane-targeted fluorescence protein to the HMM surface. Scale bar is 10 μm.

axial resolution for a broadband spectrum (see Figure 1d and Figure S4).

Figure 2a shows the experimental setup for MAPM, where a traditional fluorescence microscope is used. Stained cell samples on top of an HMM and a glass substrate (see Methods for details) were illuminated by a 488 nm CW laser (Coherent Genesis MX488-1000 STM) with an intensity of approximately 23 W/cm^2. The HeLa cells were seeded onto the HMM substrate (see Figure S5) and cover glass substrates, and passaged cells were transfected and incubated (see Methods for details). The HeLa cells were labeled with two plasma-membrane-targeted fluorescent protein fusions Lyn-TagRFP-T and AKAR4-Kras as markers that allowed us to spectrally separate their signals and localize their locations within the plasma membrane.[41,42] The fluorescent signal was collected by an objective and a magnification tube lens (40× 2/0.6 NA, 100× 2/1.49 NA Olympus objective), and then sent to the camera (Hamamatsu ORCA-Flash 4.0 V3) with proper excitation and emission filter configurations (see Methods for details).

Photobleaching response of the fluorescent proteins refers to the emission intensity decrease as time goes by, from which a lifetime mapping can be extracted by a mathematical fitting of photobleaching response in each pixel as a function of time. Figure 2b shows a typical fluorescence microscope image stack consisting of 500 frames of images (1 frame per second) in order to obtain a complete photobleaching decay curve at most of the pixels of the wide-field images. We show a few examples of the decay curves in Figure 2c, which are individually fitted using an exponential fitting MATLAB code to obtain the corresponding photobleaching lifetime (see Methods for details). Here, we assume that the bleaching response is a single exponential decay under low-intensity illumination by a CW laser.[36,40] A constant laser intensity of 23 W/cm^2 is applied for all the wide-field illuminations in our MAPM experiments to exclude the excitation power dependence factor of photobleaching.

HeLa cells are used for the demonstration of MAPM. A typical fluorescence intensity image of a Hela cell is shown in Figure 3a, where a 520/40 nm band-pass filter was applied for this single-color image. There are two main steps to obtain the super-axial-resolution image of the Hela cell using MAPM, that is, the reconstruction of photobleaching lifetime and the conversion of distance to substrate. Figure 3b shows the

https://dx.doi.org/10.1021/acs.nanolett.0c02056
Nano Lett. XXXX, XXX, XXX−XXX

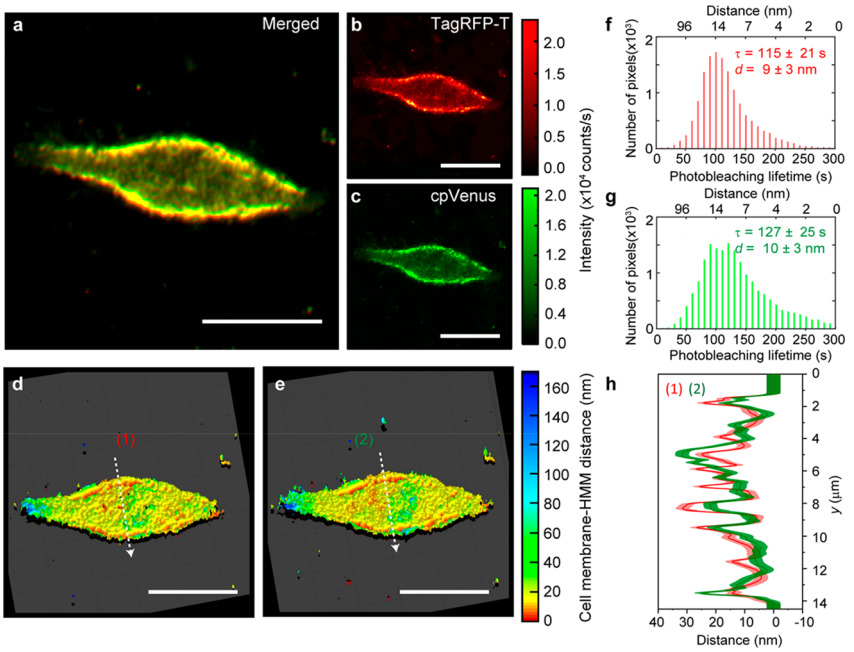

Figure 4. Dual-color MAPM images. (a–c) Dual-color fluorescence intensity images of Hela cells. Fluorescence in the TagRFP-T and cpVenus channels are shown in the red and green, respectively. (d,e) Super-axial-resolution MAPM images of these Hela cells. (f,g) Histograms of the photobleaching lifetime. (h) Distance profiles for (1) and (2) in (d) and (e), respectively. The shaded areas mark the 1σ-regions of the distance values. Scale bar is 20 μm.

photobleaching-lifetime image of the HeLa cell by the MAPM reconstruction as described above (Figure 2). We clearly observe a strong spatial dependence of the photobleaching lifetime, and we attribute it to the difference in the distance to the HMM substrate as discussed above (Figure 1). Therefore, the distance of the Hela cell membrane-targeted fluorescent protein to the HMM surface can be extracted according to the calculated axial-distance dependence of the photobleaching lifetime given in Figure 1d, and the resultant super-axial-resolution image is shown in Figure 3c. The intensity distribution is used for discriminating background signal. We eliminated the regions with no cells where the emission intensity did not exceed the background level (see Methods for details). From the control experiment with glass substrate samples, we checked and considered several effects that might affect intensity changes besides photobleaching of a fluorophore over detection time. We used the same excitation power, exposure time, buffer condition, density of chromophores, and measurement conditions during 500 frames collection with the same detection time scale for each measurement set.

More MAPM images of Hela cells are shown in Figure S6 to reveal the cell membrane's 3D profile near the substrate with an excellent axial resolution, manifesting MAPM as a potential tool for the study of the cell's interfacial morphology. First of all, we observe that the mean distance of the HeLa cell membrane from the substrate varies from 5 to 160 nm, which is in good agreement with the reported distance variation between 9 and 255 nm.[13,16,17,43−45] The cell−substrate mean distance distribution could be due to the variations in adhesion strength or the spatial heterogeneity of the cell.[46] In separation-dependent energy transfer microscopy, the axial resolution is determined by the number of photons detected[16] and characteristic curve−distance-dependent energy transfer rate. To investigate the localization accuracy of MAPM, axial distance-dependent standard errors of the mean (s.e.m., σ) are obtained in our experiment (see Supporting Information S5 and Figure S7). We obtained ∼2.4 nm localization accuracy at 1.03×10^4 initial photon counts per pixel (see Supporting Information S5). All of these 3D images unambiguously demonstrate that our MAPM is a cell imaging technology with axial resolution down to 2.4 nm. We also want to emphasize that this resolution is obtained on an HMM substrate with about 2 nm surface roughness (see Figures S5 and S8), indicating the possibility to achieve subnanometer resolution if an atomically flat HMM sample is available.

Having discussed the basic principle and demonstrated its super-axial-resolution, we now turn to the multicolor imaging capability of MAPM enabled by the unprecedented broadband Purcell effect of HMMs. To this end, two fluorescent protein fusions, Lyn-TagRFP-T (red) and AKAR4-Kras containing a circularly permutated Venus (cpVenus) (green) which are well separated in spectrum, are used to label the Hela cells for the dual-color MAPM imaging. The dual-color MAPM images are summarized in Figure 4, which clearly shows the spatial heterogeneity of photobleaching response for two fluorescence proteins located at different locations of the plasma membrane of HeLa cells. To spatially resolve the fluorescent proteins, fluorescence signals were collected by two sCMOS cameras with proper color filters. Here, we used a 550 nm bandpass filter for CH1 (Figure 4b) to collect the TagRFP-T fluorescence signal, while for CH2 (Figure 4c) a 520/40 nm band-pass filter was used to collect the cpVenus fluorescence signal. In the control experiments using a glass substrate, we observed intrinsic optical properties and photobleaching responses of TagRFP-T and cpVenus fluorescent proteins occurring during our detection time range. We checked the reproducibility of our photobleaching lifetime mapping with 20 different HeLa cells both on glass and HMM substrates. We observed that cpVenus shows a slightly faster photobleaching

https://dx.doi.org/10.1021/acs.nanolett.0c02056
Nano Lett. XXXX, XXX, XXX−XXX

response than that of TagRFP-T for high illumination power. In order to eliminate the effect of the intrinsic photophysical propertie difference between cpVenus and TagRFP-T, illumination power-dependent photobleaching behavior was measured on a glass substrate as a control experiment (see Figure S11). With excitation intensity of 23 W/cm^2, which does not show a difference of photobleaching response for CH1 and CH2, the dual-color-three-dimensional imaging reconstruction was performed.

Measuring the photobleaching lifetimes of the two fluorophores allows the determination of the distance of both proteins from the HMM surface. The height difference immediately yields the separation between the TagRFP-T and cpVenus fluorophores. In Figure 4d,e, the spatial heterogeneity of photobleaching responses and corresponding distance differences are clearly shown for different fluorescence proteins located at the different spatial location of the plasma membrane. The corresponding histograms of photobleaching lifetimes and distance for individual pixels are shown in Figure 4f,g. Figure 4h shows that the red channel and green channel have different height profiles along the cross-section line (1) and (2) in Figure 4d,e, showing an axial distance difference of nearly 0.8 nm between the tagged locations of two different fluorescence protein reporters in the membrane.

As demonstrated above, the proposed MAPM offers a new means to measure cellular adhesion and cell migration in biological applications, which does not require specialized fluorescent labels.[15−17,43] Compared with fluorescence lifetime-based microscopies[15−18,43] which rely on the time-correlated single-photon counting (TCSPC) technique to measure the nanosecond lifetime using a point scanning confocal microscope equipped with a single-photon detector, the conventional wide-field fluorescent microscope can perform the MAMP. The use of HMMs builds up a direct connection between the photobleaching speed of a fluorophore and its separation to the HMMs, thus leading to a superior axial resolution. Although it sacrifices the ability of single-molecule detection to harness an ensemble averaging to get the finer axial resolution, the MAPM supports multicolor imaging in a wide visible spectral range due to the broadband Purcell factor enhancement of HMMs.

In conclusion, we demonstrated a multicolor fluorescence imaging technique with an axial resolution down to ∼2.4 nm, which we named MAPM. We determined the axial distance of fluorescence proteins to the underneath HMM substrate with modified photobleaching dynamics of the fluorophores by the HMMs using standard fluorescence microscopy. The axial resolution may be extended to subnanometer level if better HMM substrate is available. It is also possible to combine the MAPM principle with other super-resolution techniques to further improve lateral resolution for a broader range of biological applications.

METHODS

Purcell Factor Calculation. The Purcell factor corresponds to the emission rate enhancement of a spontaneous emitter inside/near a cavity or plasmonic structure. Finite-difference time-domain (FDTD, Lumerical) simulations were performed to calculate the dispersion of the Purcell factor. By placing a dipole source on top of HMM film at $z = d$, the power emitted from the dipole in the presence of HMM/glass divided by the power emitted from the dipole in the absence of HMM/glass is calculated at wavelengths in the visible range (300−650 nm). The dipole emitter orientation within the cell membrane was assumed as random orientation. The geometries of the HMM structure in the simulations were designed to match with those displayed in Figure S5. The theoretical calculation considers all the details of the optical properties of the glass coverslip substrate/three pair of (10 nm Ag/4 nm SiO_2) multilayer HMM structure. A minimum mesh step size of 0.25 nm is defined, and the perfectly matched layers boundary conditions are adopted.

Multilayer HMM Fabrication. Ag/SiO_2 multilayer HMM, composed of 3 pairs of 10 nm Ag and 4 nm SiO_2 layers, was prepared by alternately DC magnetron sputtering and RF magnetron sputtering at room temperature. Sputtering rates for Ag and SiO_2 at 200 W were ∼1 nm/s and ∼0.8 nm/min, respectively. The pressure of the chamber was 2.5 × 10^{-6} mTorr and the Ar pressure was at 3.2 mTorr for Ag and 5 mTorr for SiO_2 during the deposition. The glass substrate (VMW Micro cover glasses, No. 1 1/2) was cleaned by acetone, IPA, and water several times and dried by compressed air. An adhesion layer (<1 nm thickness) of Cr was deposited on the substrate prior to the deposition of Ag-SiO_2 multilayer. The sputtering machine is Denton discovery 635 at Nano3 facility at Calit2, UCSD.

HeLa Cell Transfection. HeLa cells were maintained in DMEM growth media (Gibco) supplemented with 10% FBS and 1% penicillin/streptomycin. Cells were seeded onto HMM substrate 24 h prior to transfection. Alternatively, cells were seeded onto standard glass coverslips. At a confluency of approximately 70%, passaged cells were transfected with approximately 250 ng of plasmid DNA each (membrane-targeted Lyn-TagRFP-T and AKAR4-Kras (containing cpVenus), both in pcDNA3 vector) using Lipofectamine 2000 and incubated for 24 h. Prior to imaging, the HeLa cells were fixed before the measurement. Cells were washed two times with DPBS and fixed using 4% paraformaldehyde (diluted 250 μL 10% PFA with 750 μL PBS) for 10 min at room temperature. After the samples were rinsed three times with DPBS, the cells were mounted.

Experimental Setup. We used home-modified fluorescence microscopy (Olympus IX83) with either upright or inverted configuration. Upon excitation with a 488 nm laser (Coherent Genesis MX-488−1000 STM) coupled into a multimode fiber (Thorlabs, core diameter: 50 μm, NA 0.2), we acquired 500 frames (1 frame per second) of emission signal and analyzed the resulting stack of images using a mathematical fitting process with homemade MATLAB code. The multimode fiber bundle was mechanically vibrated with two 50 Hz motors in order to scramble the fiber mode, and thus reduce its spatial coherence and smooth the speckle pattern. The substrate with biological samples is illuminated with an intensity of approximately 23 W/cm^2. The cells were stained with a membrane-staining fluorophore, which emits photons in the visible spectrum. We found a neighboring area and focused using fluorescence. Then we moved to the area that we want to take the image. The fluorescent signal is collected by an objective lens (40× 2/0.6 NA Olympus objective), sent to the camera with proper laser filters. For single-colored image, 488 dichroic mirror (Di03-R488, Semrock) and a 520/40 nm band-pass filter were used to remove the TagRFP-T fluorescence contribution from the emission. For dual-color image, data recording was performed with dual-color imaging setup. The fluorescent signal is sent to two sCMOS cameras (Hamamatsu ORCA_Flash4.0 V3 digital

https://dx.doi.org/10.1021/acs.nanolett.0c02056
Nano Lett. XXXX, XXX, XXX−XXX

CMOS camera (C13440-20CU)) with proper laser filters. We used 550 nm bandpass filter (BrightLine FF01-550/88, Semrock) for CH1 to collect TagRFP-T fluorescence signal. For CH2, 520/40 nm band-pass filter was used to collect cpVenus signal from the AKAR4-Kras (CFP/YFP: cpVenus). To synchronize all equipment properly, we use Matlab software to control a DAQ voltage output module (NI-9263) from National Instruments.

Mathematical Fitting. A three-dimensional cellular picture is extracted from the data set by recording the fluorescence intensity in each pixel as a function of time and calculating the mean of the resulting distribution. For each pixel, fitting of photobleaching behavior $f = f_0 + A_{ij} \exp(-t/\tau_{ij})$. Focusing the excitation light with a 0.6 NA/1.49 NA objective lens onto the top surface of substrate allowed us to excite only molecules that are located within 450 nm/150 nm distance above the sample surface. The intensity distribution is used for discriminating background signal (BG). We eliminated the regions with no cells where the emission intensity did not exceed the background level.

$$C_{ij} = 0 \text{ if } f_0 + A_{ij} < \mathrm{BG}$$

$$C_{ij} = 1 \text{ if } f_0 + A_{ij} \geq \mathrm{BG}$$

Photobleaching lifetime

$$C \times \tau(s) = \begin{pmatrix} C_{1,1} \times \tau_{1,1} & \cdots & C_{1,1024} \times \tau_{1,1024} \\ \vdots & \ddots & \vdots \\ C_{1024,1} \times \tau_{1024,1} & \cdots & C_{1024,1024} \times \tau_{1024,1024} \end{pmatrix}$$

■ ASSOCIATED CONTENT

Supporting Information

The Supporting Information is available free of charge at https://pubs.acs.org/doi/10.1021/acs.nanolett.0c02056.

(S1) Relative photobleaching rate on hyperbolic metamaterial; (S2) Purcell factor and LDOS on single metallic film and HMM; (S3) multilayer HMM; (S4) superaxial-resolution image of the Hela cells; (S5) control experiment 1, localization accuracy of MAPM; (S6) control experiment 2, power-dependent photobleaching on glass substrate; (S7) control experiment 3, spatial uniformity of the excitation intensity; (S8) superaxial-resolution image of microtubules of Cos-7 cell (PDF)

■ AUTHOR INFORMATION

Corresponding Author

Zhaowei Liu − *Department of Electrical and Computer Engineering and Materials Science and Engineering, University of California, San Diego, La Jolla, California 92093, United States*; Email: zhaowei@ucsd.edu

Authors

Yeon Ui Lee − *Department of Electrical and Computer Engineering, University of California, San Diego, La Jolla, California 92093, United States*; orcid.org/0000-0001-8857-1251

Junxiang Zhao − *Department of Electrical and Computer Engineering, University of California, San Diego, La Jolla, California 92093, United States*

Gary C. H. Mo − *Department of Pharmacology, University of California, San Diego, La Jolla, California 92093, United States; Department of Pharmacology, University of Illinois at Chicago, Chicago, Illinois 60612, United States*

Shilong Li − *Department of Electrical and Computer Engineering, University of California, San Diego, La Jolla, California 92093, United States*

Guangru Li − *Department of Electrical and Computer Engineering, University of California, San Diego, La Jolla, California 92093, United States*

Qian Ma − *Department of Electrical and Computer Engineering, University of California, San Diego, La Jolla, California 92093, United States*; orcid.org/0000-0002-7667-332X

Qingqing Yang − *Materials Science and Engineering, University of California, San Diego, La Jolla, California 92093, United States*

Ratnesh Lal − *Materials Science and Engineering and Department of Bioengineering, University of California, San Diego, La Jolla, California 92093, United States*

Jin Zhang − *Department of Pharmacology, University of California, San Diego, La Jolla, California 92093, United States*; orcid.org/0000-0001-7145-7823

Complete contact information is available at: https://pubs.acs.org/10.1021/acs.nanolett.0c02056

Author Contributions

Y.U.L. and Z.L. conceived and designed the experiment. Y.U.L. and J.Z. performed the experiments. G.C.H.M. prepared biological samples. Y.U.L. and S.L. developed the algorithm and wrote the codes for image processing. G.L. and Q.M. fabricated HMM samples. Q.Y. performed the AFM measurement. Y.U.L. performed simulations, data analysis, and wrote the manuscript which was revised by all authors.

Notes

The authors declare no competing financial interest.

■ ACKNOWLEDGMENTS

This work was supported by the Gordon and Betty Moore Foundation and the National Science Foundation (CBET1604216).

■ REFERENCES

(1) Huang, B.; Wang, W.; Bates, M.; Zhuang, X. Three-Dimensional Super-Resolution Imaging by Stochastic Optical Reconstruction Microscopy. *Science* **2008**, *319*, 810−813.

(2) Schermelleh, L.; Carlton, P. M.; Haase, S.; Shao, L.; Winoto, L.; Kner, P.; Burke, B.; Cardoso, M. C.; Agard, D. A.; Gustafsson, M. G. L.; et al. Subdiffraction Multicolor Imaging of the Nuclear Periphery with 3D Structured Illumination Microscopy. *Science* **2008**, *320*, 1332−1336.

(3) Hell, S. W.; Wichmann, J. Breaking the Diffraction Resolution Limit by Stimulated Emission: Stimulated-Emission-Depletion Fluorescence Microscopy. *Opt. Lett.* **1994**, *19*, 780.

(4) Fölling, J.; Bossi, M.; Bock, H.; Medda, R.; Wurm, C. A.; Hein, B.; Jakobs, S.; Eggeling, C.; Hell, S. W. Fluorescence Nanoscopy by Ground-State Depletion and Single-Molecule Return. Nat. *Nat. Methods* **2008**, *5*, 943−945.

(5) Betzig, E.; Patterson, G. H.; Sougrat, R.; Lindwasser, O. W.; Olenych, S.; Bonifacino, J. S.; Davidson, M. W.; Lippincott-Schwartz, J.; Hess, H. F. Imaging Intracellular Fluorescent Proteins at Nanometer Resolution. *Science* **2006**, *313*, 1642−1645.

(6) Rust, M. J.; Bates, M.; Zhuang, X. Sub-Diffraction-Limit Imaging by Stochastic Optical Reconstruction Microscopy (STORM). *Nat. Methods* **2006**, *3*, 793−796.

(7) Gustafsson, M. G. Surpassing the Lateral Resolution Limit by a Factor of Two Using Structured Illumination Microscopy. *J. Microsc.* **2000**, *198*, 82−87.
(8) Gustafsson, M. G. L.; Shao, L.; Carlton, P. M.; Wang, C. J. R.; Golubovskaya, I. N.; Cande, W. Z.; Agard, D. A.; Sedat, J. W. Three-Dimensional Resolution Doubling in Wide-Field Fluorescence Microscopy by Structured Illumination. *Biophys. J.* **2008**, *94*, 4957−4970.
(9) Böhm, U.; Hell, S. W.; Schmidt, R. 4Pi-RESOLFT Nanoscopy. *Nat. Commun.* **2016**, *7*, 10504.
(10) Xu, K.; Babcock, H. P.; Zhuang, X. Dual-Objective STORM Reveals Three-Dimensional Filament Organization in the Actin Cytoskeleton. Nat. *Nat. Methods* **2012**, *9*, 185−188.
(11) Jia, S.; Vaughan, J. C.; Zhuang, X. Isotropic Three-Dimensional Super-Resolution Imaging with a Self-Bending Point Spread Function. Nat. *Nat. Photonics* **2014**, *8*, 302−306.
(12) Shtengel, G.; Galbraith, J. A.; Galbraith, C. G.; Lippincott-Schwartz, J.; Gillette, J. M.; Manley, S.; Sougrat, R.; Waterman, C. M.; Kanchanawong, P.; Davidson, M. W.; et al. Interferometric Fluorescent Super-Resolution Microscopy Resolves 3D Cellular Ultrastructure. *Proc. Natl. Acad. Sci. U. S. A.* **2009**, *106*, 3125−3130.
(13) Kanchanawong, P.; Shtengel, G.; Pasapera, A. M.; Ramko, E. B.; Davidson, M. W.; Hess, H. F.; Waterman, C. M. Nanoscale Architecture of Integrin-Based Cell Adhesions. *Nature* **2010**, *468*, 580−584.
(14) Förster, T. Zwischenmolekulare Energiewanderung Und Fluoreszenz. *Ann. Phys.* **1948**, *437*, 55−75.
(15) Berndt, M.; Lorenz, M.; Enderlein, J.; Diez, S. Axial Nanometer Distances Measured by Fluorescence Lifetime Imaging Microscopy. *Nano Lett.* **2010**, *10*, 1497−1500.
(16) Chizhik, A. I.; Rother, J.; Gregor, I.; Janshoff, A.; Enderlein, J. Metal-Induced Energy Transfer for Live Cell Nanoscopy. Nat. *Nat. Photonics* **2014**, *8*, 124−127.
(17) Chizhik, A. M.; Ruhlandt, D.; Pfaff, J.; Karedla, N.; Chizhik, A. I.; Gregor, I.; Kehlenbach, R. H.; Enderlein, J. Three-Dimensional Reconstruction of Nuclear Envelope Architecture Using Dual-Color Metal-Induced Energy Transfer Imaging. *ACS Nano* **2017**, *11*, 11839−11846.
(18) Chizhik, A. M.; Wollnik, C.; Ruhlandt, D.; Karedla, N.; Chizhik, A. I.; Hauke, L.; Hähnel, D.; Gregor, I.; Enderlein, J.; Rehfeldt, F. Dual-Color Metal-Induced and Förster Resonance Energy Transfer for Cell Nanoscopy. *Mol. Biol. Cell* **2018**, *29*, 846−851.
(19) Smith, D. R.; Pendry, J. B.; Wiltshire, M. C. K. Metamaterials and Negative Refractive Index. *Science* **2004**, *305*, 788−792.
(20) Pendry, J. B.; Martín-Moreno, L.; Garcia-Vidal, F. J. Mimicking Surface Plasmons with Structured Surfaces. *Science* **2004**, *305*, 847−848.
(21) Poddubny, A.; Iorsh, I.; Belov, P.; Kivshar, Y. Hyperbolic Metamaterials. Nat. *Nat. Photonics* **2013**, *7*, 948−957.
(22) Shekhar, P.; Atkinson, J.; Jacob, Z. Hyperbolic Metamaterials: Fundamentals and Applications. *Nano Converg.* **2014**, *1*, 14.
(23) Liu, Z.; Lee, H.; Xiong, Y.; Sun, C.; Zhang, X. Far-Field Optical Hyperlens Magnifying Sub-Diffraction-Limited Objects. *Science* **2007**, *315*, 1686.
(24) Sun, J.; Shalaev, M. I.; Litchinitser, N. M. Experimental Demonstration of a Non-Resonant Hyperlens in the Visible Spectral Range. *Nat. Commun.* **2015**, *6*, 7201.
(25) Jacob, Z.; Smolyaninov, I. I.; Narimanov, E. E. Broadband Purcell Effect: Radiative Decay Engineering with Metamaterials. *Appl. Phys. Lett.* **2012**, *100*, 181105.
(26) Lu, D.; Kan, J. J.; Fullerton, E. E.; Liu, Z. Enhancing Spontaneous Emission Rates of Molecules Using Nanopatterned Multilayer Hyperbolic Metamaterials. *Nat. Nanotechnol.* **2014**, *9*, 48−53.
(27) Krishnamoorthy, H. N. S.; Jacob, Z.; Narimanov, E.; Kretzschmar, I.; Menon, V. M. Topological Transitions in Metamaterials. *Science* **2012**, *336*, 205−209.
(28) Jacob, Z.; Kim, J.-Y.; Naik, G. V.; Boltasseva, A.; Narimanov, E. E.; Shalaev, V. M. Engineering Photonic Density of States Using Metamaterials. *Appl. Phys. B: Lasers Opt.* **2010**, *100*, 215−218.
(29) Enderlein, J. Single-Molecule Fluorescence near a Metal Layer. *Chem. Phys.* **1999**, *247*, 1−9.
(30) Ferrari, L.; Lu, D.; Lepage, D.; Liu, Z. Enhanced Spontaneous Emission inside Hyperbolic Metamaterials. Opt. *Opt. Express* **2014**, *22* (4301), 4301.
(31) Song, L.; Hennink, E. J.; Young, I. T.; Tanke, H. J. Photobleaching Kinetics of Fluorescein in Quantitative Fluorescence Microscopy. *Biophys. J.* **1995**, *68*, 2588−2600.
(32) Ferrari, L.; Wu, C.; Lepage, D.; Zhang, X.; Liu, Z. Hyperbolic Metamaterials and Their Applications. *Prog. Quantum Electron.* **2015**, *40*, 1−40.
(33) Lee, Y. U.; Gaudin, O. P. M. M.; Lee, K.; Choi, E.; Placide, V.; Takaishi, K.; Muto, T.; André, P.; Muranaka, A.; Uchiyama, M.; et al. Organic Monolithic Natural Hyperbolic Material. *ACS Photonics* **2019**, *6*, 1681−1689.
(34) Zhang, Y.; Aslan, K.; Malyn, S. N.; Geddes, C. D. Metal-Enhanced Phosphorescence (MEP). *Chem. Phys. Lett.* **2006**, *427*, 432−437.
(35) Zhang, Y.; Aslan, K.; Previte, M. J. R.; Geddes, C. D. Metal-Enhanced Singlet Oxygen Generation: A Consequence of Plasmon Enhanced Triplet Yields. *J. Fluoresc.* **2007**, *17*, 345−349.
(36) Vasilev, K.; Stefani, F. D.; Jacobsen, V.; Knoll, W.; Kreiter, M. Reduced Photobleaching of Chromophores Close to a Metal Surface. *J. Chem. Phys.* **2004**, *120*, 6701−6704.
(37) Muthu, P.; Gryczynski, I.; Gryczynski, Z.; Talent, J.; Akopova, I.; Jain, K.; Borejdo, J. Decreasing Photobleaching by Silver Island Films: Application to Muscle. *Anal. Biochem.* **2007**, *366*, 228−236.
(38) Malicka, J.; Gryczynski, I.; Fang, J.; Kusba, J.; Lakowicz, J. R. Photostability of Cy3 and Cy5-Labeled DNA in the Presence of Metallic Silver Particles. *J. Fluoresc.* **2002**, *12*, 439−447.
(39) Zaiba, S.; Lerouge, F.; Gabudean, A.-M.; Focsan, M.; Lermé, J.; Gallavardin, T.; Maury, O.; Andraud, C.; Parola, S.; Baldeck, P. L. Transparent Plasmonic Nanocontainers Protect Organic Fluorophores against Photobleaching. *Nano Lett.* **2011**, *11*, 2043−2047.
(40) Cang, H.; Liu, Y.; Wang, Y.; Yin, X.; Zhang, X. Giant Suppression of Photobleaching for Single Molecule Detection via the Purcell Effect. *Nano Lett.* **2013**, *13*, 5949−5953.
(41) Depry, C.; Allen, M. D.; Zhang, J. Visualization of PKA Activity in Plasma Membrane Microdomains. *Mol. BioSyst.* **2011**, *7*, 52−58.
(42) Mo, G. C. H. H.; Ross, B.; Hertel, F.; Manna, P.; Yang, X.; Greenwald, E.; Booth, C.; Plummer, A. M.; Tenner, B.; Chen, Z.; et al. Genetically Encoded Biosensors for Visualizing Live-Cell Biochemical Activity at Super-Resolution. Nat. *Nat. Methods* **2017**, *14*, 427−434.
(43) Baronsky, T.; Ruhlandt, D.; Brückner, B. R.; Schäfer, J.; Karedla, N.; Isbaner, S.; Hähnel, D.; Gregor, I.; Enderlein, J.; Janshoff, A.; et al. Cell−Substrate Dynamics of the Epithelial-to-Mesenchymal Transition. *Nano Lett.* **2017**, *17*, 3320−3326.
(44) Kuss, S.; Polcari, D.; Geissler, M.; Brassard, D.; Mauzeroll, J. Assessment of Multidrug Resistance on Cell Coculture Patterns Using Scanning Electrochemical Microscopy. *Proc. Natl. Acad. Sci. U. S. A.* **2013**, *110*, 9249−9254.
(45) Paszek, M. J.; DuFort, C. C.; Rubashkin, M. G.; Davidson, M. W.; Thorn, K. S.; Liphardt, J. T.; Weaver, V. M. Scanning Angle Interference Microscopy Reveals Cell Dynamics at the Nanoscale. Nat. *Nat. Methods* **2012**, *9*, 825−827.
(46) Bourg, N.; Mayet, C.; Dupuis, G.; Barroca, T.; Bon, P.; Lécart, S.; Fort, E.; Lévêque-Fort, S. Direct Optical Nanoscopy with Axially Localized Detection. Nat. *Nat. Photonics* **2015**, *9*, 587−593.

https://dx.doi.org/10.1021/acs.nanolett.0c02056
Nano Lett. XXXX, XXX, XXX−XXX